

# Passive Gust Alleviation of a Flying-wing Aircraft by Analysis and Wind-tunnel Test of a Scaled Model in Dynamic Similarity

Shun He, Shijun Guo<sup>\*</sup>, Ying Liu, Wukui Luo

Centre for Aeronautics, Cranfield University, Cranfield, Bedford, UK, MK43 0AL

---

## Abstract

An investigation was conducted to evaluate the effectiveness of a passive gust alleviation device (PGAD) installed in a flying-wing aircraft of 62.3m wing span at large swept back angle. It was performed by numerical analysis and validated by wind-tunnel test of a 1:25 reduced scale physical model of dynamic similarity to the full-scale aircraft. The 1-cosine gust model with a range of gust parameters specified in the airworthiness regulation CS-23 was taken in the gust response analysis that led to 7~9% gust alleviation results by employing the PGAD. The gust response dominated by the first three modes of the aircraft was most critical in the frequency close to the first bending mode of the wing. The wind-tunnel test model was designed and manufactured based on dynamic scaling law, and proved to be of excellent dynamic similarity by the deviation of less than 5.5% between the first three modes of the physical model measured by vibration test and the full-scale aircraft model. The wind tunnel test results show that the gust response of the model in the specified range was reduced by 8.3~14.3% according to the measured wing tip deflection associated with the PGAD oscillation amplitude at 4.0°~15.5°. The present study shows that the numerical analysis of gust response and alleviation of a full-scale aircraft installed with PGAD can be validated by wind tunnel test of a scaled physical model with dynamic similarity.

*Keywords:* Flying-wing aircraft, Passive gust alleviation, Dynamic similarity, Wind-tunnel test

---

---

<sup>\*</sup> Corresponding author.

Email addresses: [s.guo@cranfield.ac.uk](mailto:s.guo@cranfield.ac.uk) (Shijun Guo)

## 1. Introduction

To improve aerodynamic efficiency and performance, a High-Altitude Long-Endurance (HALE) aircraft normally adopt a tailless flying-wing configuration with high aspect ratio (APR) wing [1,2]. As a consequence, the wing structural flexibility and response to gust load will increase and lead to degradation of aeroelastic stability, flight controllability and structure failure [3]. Although carbon/epoxy composite materials of high specific modulus and strength [4] are usually employed to enhance the structure integrity, gust load alleviation is of great importance for such lightweight and flexible wing structures.

Passive and active technologies for gust alleviation have been investigated in previous research and some applications. Gust alleviation of an aircraft by active control is normally operated through the wing leading edge (LE) or trailing edge control surfaces where advanced flight control systems [5] can be employed. The Active Lift Distribution Control System developed in C-5A Galaxy is generally considered as the first application of active gust alleviation strategy [6], where bending moment of the wing was reduced by using the aileron as the control device. Gust response was successfully reduced by 50% for the B-2 Stealth Bomber by combining the elevators and gust load alleviation surfaces [7]. According to Frederick et al. [6], 81% gust load reduction was achieved for a wind turbine blade with a rapidly actuated trailing-edge flap by using simple feedback control. Making use of the piezoelectric transducer, gust load alleviation with considerable attenuation of bending moment at the wing root was numerically and experimentally studied by Versiani et al. [8]. A mixed feedforward and feedback control was investigated by Alam et al. [9] on a lightweight flexible blended-wing-body aircraft. The results showed that the gust load alleviation system was significantly improved with the engagement of the feedforward controller. Li and Qin [10] used circulation control via blowing over airfoil trailing-edge to alleviate the gust load. The numerical simulation showed that the circulation control can effectively alter the lift disturbance caused by gust, while keep the lift coefficient constant by imposing dynamically adaptive momentum coefficient of the jet flow.

As an alternative means, passive control system is considered as a simpler, more reliable and potentially more efficient approach for gust alleviation although it is usually designed to respond in a narrow frequency band. A classical passive system was proposed by Roesch and Harlan [11] for gust load alleviation by making use of the coupling between flaps and a couple of mass balanced auxiliary wing. In this study, only vertical gust was considered and satisfactory result of gust alleviation was achieved. Passive gust alleviation has attracted more attentions in recent years when developing unmanned air vehicles of various configurations and flexible airframes to meet aeroelastic challenge. A passive twist wing-tip as a gust alleviation device was studied in 2008 by Miller et al. [12,13] for a jointed-wing sensor-craft. Numerical analysis has demonstrated the effectiveness of the device for gust response alleviation of the sensor-craft and also a large transport aircraft by Guo et al. [14,15] subject to the aeroelastic stability constraint. Castrichini et al. [16,17] proposed a passive folding wing-tip with a nonlinear spring to allow the device response to excessive loads. Significant gust reduction was also achieved according to the numerical analysis. Wind tunnel test of a prototype model of the passive folding wing-tip was conducted by Cheung et al. [18,19] to reveal the effectiveness of the device for gust load alleviation.

The passive twist wing-tip has been further developed as a specific device, known as Passive Gust Alleviation Device (PGAD), for gust alleviation of a flying-wing aircraft [14,15,20]. In the initial study, attention was focused on optimization of the flying-wing aircraft and the key parameters of the PGAD design subject to multi-constraints [14]. The study was later extended to the influence of the PGAD on the body freedom flutter of a scaled flying-wing aircraft [20]. Since the benefit and effectiveness of the PGAD has been well evaluated by numerical analysis, a forward step is necessary to demonstrate the feasibility of employing PGAD for gust alleviation by experiment.

A physical scaled model is usually taken in wind tunnel test to measure aerodynamic characteristics of the original full-scale wing or aircraft. To measure the aeroelastic response of a wing or aircraft through wind tunnel test however, the scaled model should be designed and built to represent the dynamic and aeroelastic characteristic of the full-scale model. Two scaling methods have been developed for such an aeroelastically scaled model for wind tunnel test. The classical method for aeroelastic scaling based on dimensional analysis was presented by Bisplinghoff et al. [21]. In this method, the stiffness and mass characteristics of the full-scale model are estimated first, and then scaled to the reduced model size according to the model scaling factors. Following this method, Yusuf et al. [22] and Allen et al. [23] created a full-scale beam model to match the stiffness of the original detailed FE model first; the stiffness and mass of a scaled wind tunnel model were subsequently obtained according to the dynamic scale factors. To satisfy the dynamic scaling requirements, varying beam cross-section and lump mass along the wing span were chosen when building the physical scaled model [22]. The second method is actually an extension of the first one by employing an optimization process to improve the design of an aeroelastically scaled wind tunnel model [24–26]. In this method, the key geometric parameters of the scaled model, such as sizes of the cross-section of a beam segment, are taken as the design variables; while the desirable static or dynamic behaviour, such as static deflection, buckling or mode shapes to match the full-scale model results, are set as the objectives; by optimizing the design variables, a minimize difference of the structural behaviours between the full-scale and reduced scale models can be obtained. The design process for stiffness and mass data was divided and operated in separate stages in the study by French and Eastep [24] where a sample wing structure was designed, manufactured and tested. A systematic study to build an aeroelastic scaled model based on this method was also carried out by Ricciardi et al [25].

In the present investigation, effort has been made to verify the numerical model and analysis applied to the flying-wing aircraft with the PGAD by wind tunnel test. Firstly, the gust response and alleviation of the full-scale flying-wing aircraft of 62.3m wing span by employing PGAD was evaluated in compliance with the airworthiness CS-23 [27]. Secondly, a 1:25 scaled model of dynamic similarity to the full-scale aircraft was designed and built to best represent the full-scale aircraft with optimized structure and the PGAD for wind tunnel test. Finally, wind-tunnel test was performed to assess the feasibility and validate the analytical method used for evaluating the PGAD gust alleviation of the flying-wing aircraft.

## **2. The flying-wing aircraft and gust alleviation with the PGAD**

### **2.1 The flying-wing aircraft and PGAD**

The full-scale flying-wing aircraft (half span planform) with the landing gears, engine and fuel tanks considered in the present study is shown in Fig.1(a), and the basic design data is listed in Table 1. The aircraft is of the feature of tailless, a large sweep angle and high aspect ratio outer wing with a PGAD of 2m length installed at each of the wing-tips as illustrated in Fig. 1(b).

The aircraft structure was divided into three sections namely the inboard wing from the centre of the body to the kink section, outboard wing and the PGAD. A multi-spar airframe layout was opted for the inboard wing, which is measured 10.8m from the body centre to the wing kink section as shown in Fig.1(a); a conventional two-spar layout was chosen for the outboard wing of high aspect ratio where the front and rear spars are located at 15% and 75% of the local chord respectively.

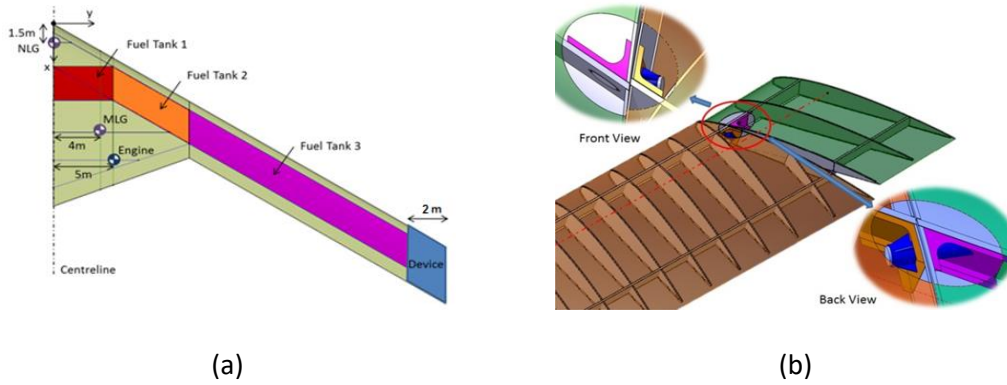


Figure 1. (a) half of the flying-wing aircraft planform and (b) the PGAD installed at the wing-tip.

Table 1. Some technical data of the flying-wing aircraft

Wing span ( <i>m</i> )	62.3	Aircraft projected area ( <i>m</i> <sup>2</sup> )	197.07
Fuselage length / wing root chord ( <i>m</i> )	14.71	Outer wing chord (from $y = 10.8$ m)	4.57
Mean chord ( <i>m</i> )	6.33	Sweep angle of LE (°)	30
MTOM (full fuel, <i>kg</i> )	55,350	OEM (empty fuel, <i>kg</i> )	23,350
Engine mass ( <i>kg</i> )	2,000	Landing gear mass ( <i>kg</i> )	2,200
Cruise speed $V_C$ ( <i>m/s</i> )	192	Diving speed $V_D$ ( <i>m/s</i> )	230
Cruise altitude ( <i>m</i> )	18300	Wing aerofoil	NACA 4415

As shown in Fig.1(b), the PGAD was mounted at the wing-tip through a shaft and a torque spring. By locating the shaft ahead of the pressure centre of the device, a nose down rotation was inherently generated as a response to the aerodynamic moment produced by gust load and counterbalanced by the spring. As a result, the passive rotation of the PGAD would reduce the excessive gust load acting on the wing. To prevent the interaction with the wing, the root section of the PGAD was in parallel to the stream line as shown Fig.1 (b). When the PGAD was locked, it acted as an integral part of a fixed wing.

## 2.2 The aerodynamic and structure analysis

The aerodynamic analysis for the whole aircraft was performed by using computational fluid dynamics (CFD) method, and compared with vortex lattice method, panel method and lifting line theory as shown in Fig. 2. The trailing edge vortex at the wing kink region as the 3D effect was captured by the CFD simulation as shown in Fig.2(a). This flow field feature revealed the significant pressure drop and caused lift reduction in the spanwise lift distribution as shown in Fig.2(b). Since this feature could not be captured by the low fidelity aerodynamic methods for this particular aircraft, the CFD method was chosen to calculate the aerodynamic force for subsequent structural analysis and optimization. An angle of attack (AoA) = 5° was set at the wing root since the maximum lift to drag coefficient ratio ( $C_L/C_D$ ) is corresponding to  $\alpha=5^\circ$  according to the drag polar of NACA4415 airfoil. The aerodynamic

force was obtained to meet the lift requirement for the aircraft at cruise Mach number 0.65 in the condition of 20% fuel consumption from the MTOM case.

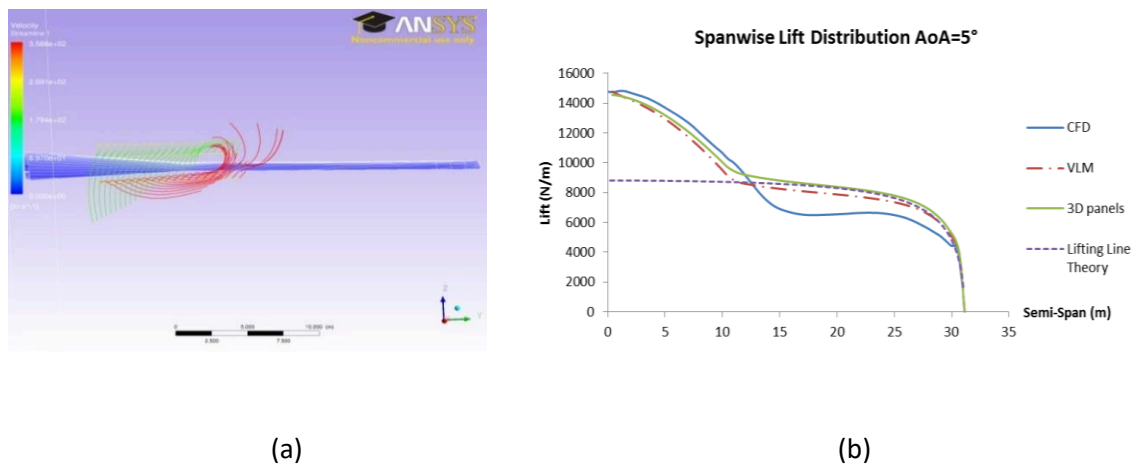


Figure 2. (a) Flow field at the wing kink region, (b) span-wise lift distribution by different methods

Based on the aerodynamic results, the wing structure was analysed and optimized subject to buckling, strength, strain and flutter constraints. The aircraft structure was made of carbon fibre composite IM7/8552 of ply thickness 0.13mm with material properties in the usual notations listed in Table 2. Symmetrical layup was adopted for the laminate of structural component such as spar and rib webs, flanges, stringers and skins.

Table 2. Mechanical property of composite material IM7/8552

$E_1$	$E_2$	$G_{12}$	$\nu_{12}$	$X_t$	$X_c$	$Y_t$	$Y_c$	S	$\rho$
(GPa)				(MPa)					( $kg/m^3$ )
164	12	5.8	0.3	2724	1690	111	250	120	1570

In the initial design, the upper and lower wing skins were reinforced by I-section stringers with pitch setting to 0.2m and 0.4m respectively. The ribs were arranged perpendicularly to the rear spar with constant pitch of 0.75m from centre to the kink and gradually increased to 1m at the tip. Several heavy ribs were included to support the concentrated load from the pylon, engine, landing gear and control devices. Both landing gear and engine were included and modelled as concentrated masses in the location as shown in Fig.1 (a). The remaining system mass was also modelled as lump mass distributed along the wing span to represent the flight control devices, fuel tanks and avionics systems. These concentrated masses were rigidly connected to the primary structures. Following the preliminary design where the component size was determined by buckling and stress analysis, a finite element (FE) model of the aircraft structure was built by using Nastran. The whole model was clamped along the body centre line.

In the FE model, the wing skins, ribs and spar webs were modelled using QUAD4 and TRIA3 shell elements; the stringers, spar caps, and rib caps were modelled using BAR element. To ensure the mesh density is adequate enough, mesh sensitivity analysis was conducted based on three models with the overall number of elements nearly doubled from Mesh 1 to Mesh 3 as listed in Table 3. The structural analysis results of the wing as shown in Table 3 indicate that the model has converged. When the model mesh density increases from Mesh 1 to Mesh 3 for example, the deflection difference is only 0.3%; the maximum failure index (FI) difference (lower skin) was reduced from 10% to 2.2%; the maximum strain difference (lower skin) was reduced from 6.7% to 3.1%.

Table 3. Mesh density and structure analysis results of the FE model

	Mesh 1	Mesh 2	Mesh 3
Nominal element size (mm)	200	150	100
Number of Elements	19169	29657	63130
Number of Nodes	11010	19334	47106
Deflection	2.56 m	2.56 m	2.55 m
Upper skin failure index (FI)	0.51	0.52	0.53
Upper skin strain	3320 $\mu\epsilon$	3460 $\mu\epsilon$	3520 $\mu\epsilon$
Lower skin failure index (FI)	0.81	0.89	0.91
Lower skin strain	5200 $\mu\epsilon$	4850 $\mu\epsilon$	4700 $\mu\epsilon$

Optimization of the wing-box structure made of carbon/epoxy was performed by using the gradient based optimizer built within Nastran. The objective is set to minimize the structural weight  $W(x)$  subject to multi constraints, which can be written in the general form of an optimization problem,

$$\begin{aligned}
 & \text{Minimize } W(x) \\
 & \text{Subject to strain} \leq 3500 \mu\epsilon \text{ (<2\% accuracy tolerance)} \\
 & FI < 1.0 \\
 & BLF \geq 1 \\
 & V_f \geq 1.15V_D
 \end{aligned} \tag{1}$$

where  $\mu\epsilon$  and  $FI$  represents the micro strain and failure index respectively,  $BLF$  is buckling factor,  $V_f$  is flutter velocity and  $V_f \geq 1.15V_D$  (the diving speed  $V_D=230$  m/s, see Table 1) is a constraint to satisfy the airworthiness requirement. By using Nastran Sol 200, the damping factor for each of the modes was calculated as part of the flutter analysis to influence the search direction of the design variables during the optimization process. The wing structure was divided to 11 sections along the span as show in Fig. 3 (a). The design variables  $x$  include the ply thickness and fibre angles of the upper and lower skins of the 11 sections. As the results, the upper skin met the buckling constraint condition under limit load, while the lower skin laminate satisfied the constraint of maximum 3500 micro strain ( $\mu\epsilon$ ). Fig. 3 (b) shows that the maximum strain is 3570  $\mu\epsilon$  within 2% deviation tolerance at the kink region.

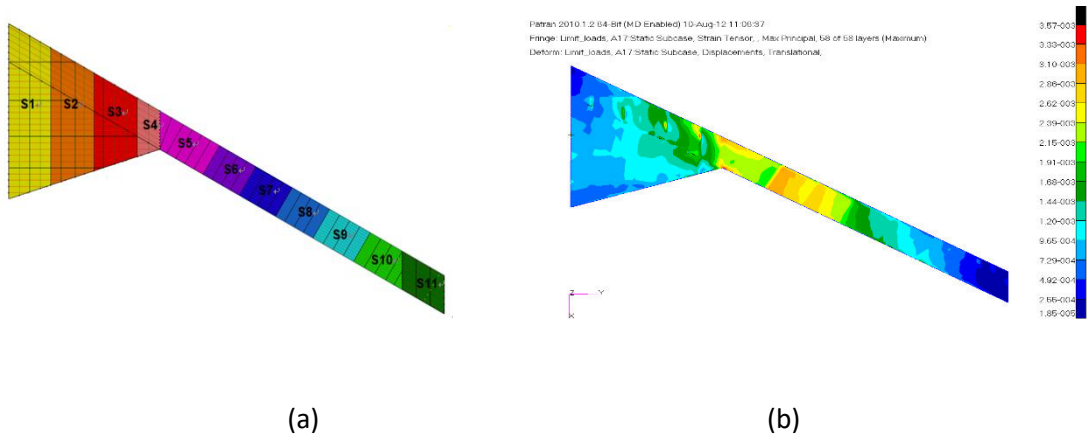


Figure 3. (a) Sections of design variable group (b) strain plot of lower skin (Maximum 3570  $\mu\epsilon$ )

For the PGAD model, the rib and skin remain the same as the optimized wing structure. The rigid bar and CELAS1 element were used to model the PGAD shaft and torque spring respectively. The shaft location, spring stiffness, mass and centre of gravity (CG) of the PGAD were identified as the key design parameters to alleviate the gust response as studied before [14,20]. In the present study, the values of these parameters for the PGAD are evaluated and shown in Table 4 where the location of the CG and shaft are measured from the LE. The study has revealed that the PGAD mass and CG has limited influence on the gust response, but plays more significant role in flutter characteristic of the wing.

Table 4. PGAD design parameters for the flying-wing aircraft

Span ( <i>m</i> )	Mass (kg)	CG (% of local chord from LE)	Shaft location (% of local chord from LE)	Spring stiffness (Nm/rad)
2	82	44.7	15	$5.8 \times 10^4$

Following the optimal design of the structures and PGAD, mode and flutter analysis was conducted to extract the dynamic and aeroelastic characteristics of the flying-wing aircraft with the PGAD integrated at the wing tip. In full-fuel condition, the first five modes that dominate the gust response and flutter speed were calculated and listed in Table 5. The flutter speed and frequency at cruising altitude were predicted as  $V_f = 356.3$  m/s and  $f_f = 3.25$  Hz as shown in Table 5, which satisfied the airworthiness requirement ( $V_f > V_D \times 1.15$  where  $V_D$  is the diving speed as listed in Table 1). In addition, the flutter speed at sea level was also predicted as  $V_f = 248.0$  m/s with frequency  $f_f = 2.93$  Hz. The  $V$ - $g$  and  $V$ - $f$  plots at sea level displayed in Fig. 4 indicate a strong coupling between the 1<sup>st</sup> bending, 2<sup>nd</sup> bending mode and the PGAD rotation mode that leads to the flutter speed  $V_f = 248.0$  m/s when the damping factor  $g$  becomes positive. As the flight speed increases, a coupling occurs between the 3<sup>rd</sup> bending mode and the 1<sup>st</sup> torsion mode that leads to the second flutter speed at  $V = 290.10$  m/s. It is obvious that the flutter is dominated by the coupling between the wing bending and torsion modes, and the PGAD rotation mode. Therefore, the CG and mass of PGAD plays a significant role for the flutter characteristic of the aircraft.

For a flying-wing aircraft, body freedom flutter (BFF) phenomenon is a special concern [20] since the BFF speed usually occurs at lower flight speed than the classical flutter speed. To ensure no BFF would happen for the present aircraft, the flutter analysis was extended to including rigid modes (heaving and pitching mode of the aircraft) and the structural modes as shown in Table 5. As the results, no body freedom flutter is observed.

Table 5. Modal and flutter analysis results of the flying-wing aircraft

Modal characteristics				
Wing 1 <sup>st</sup> bending	PGAD rotation	Wing 2 <sup>nd</sup> bending	Wing 3 <sup>rd</sup> bending	Wing 1 <sup>st</sup> torsion
0.70 Hz	1.93 Hz	3.34 Hz	7.08 Hz	12.87 Hz
Flutter characteristic				
		Sea level		Cruise altitude
	Flutter speed	248.0 m/s		356.3 m/s
	Flutter frequency	2.93 Hz		3.25 Hz

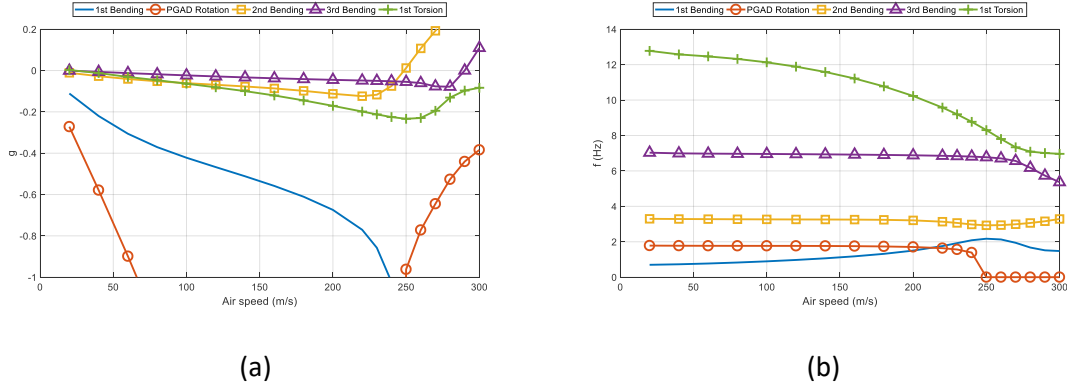


Figure 4. Flutter speed and frequency of the flying-wing aircraft at sea level: (a) V-g plot (b) V-f plot.

### 2.3 The gust response analysis

A general form of the governing equation for aeroelastic analysis of the aircraft is expressed below.

$$\mathbf{M}\ddot{\mathbf{x}} + \mathbf{D}\dot{\mathbf{x}} + \mathbf{K}\mathbf{x} = \mathbf{F}_A + \mathbf{F}_g \quad (2)$$

where  $\mathbf{M}$ ,  $\mathbf{D}$  and  $\mathbf{K}$  represents the mass, damping and stiffness matrix of the aircraft structure respectively;  $\mathbf{x}$  represents the special displacement vector;  $\mathbf{F}_A$  and  $\mathbf{F}_g$  represents the unsteady aerodynamic force vector due to dynamic motion and gust load input respectively, which are calculated using the Doublet-Lattice Method (DLM) in the Nastran package. As part of the wing structure, the PGAD is included in the  $\mathbf{M}$  and  $\mathbf{K}$  model and also the  $\mathbf{F}_A$  and  $\mathbf{F}_g$  calculations.

By employing the normal mode method,

$$\mathbf{x} = \boldsymbol{\phi}\mathbf{q} \quad (3)$$

where  $\boldsymbol{\phi}$  is the mode shape,  $\mathbf{q}$  is the generalized coordinate vector, Eq. (2) can be rewritten in generalized coordinate system and transferred from time-domain to frequency-domain as below.

$$-\omega^2 \bar{\mathbf{M}}\mathbf{q} + i\omega \bar{\mathbf{D}}\mathbf{q} + \bar{\mathbf{K}}\mathbf{q} = \bar{\mathbf{F}}_A + \bar{\mathbf{F}}_g \quad (4)$$

where  $\bar{\mathbf{M}}$ ,  $\bar{\mathbf{D}}$  and  $\bar{\mathbf{K}}$  represent the generalized mass, damping and stiffness matrix of the wing structure respectively, and

$$\bar{\mathbf{F}}_A = q_\infty \bar{\mathbf{Q}}_A \mathbf{q} \quad (5)$$

$$\bar{\mathbf{F}}_g = q_\infty P(\omega) \bar{\mathbf{Q}}_g \mathbf{w}(\omega)$$

where  $q_\infty$  is the dynamic pressure,  $P(\omega)$  is the frequency variation of the gust according to the discrete gust profile;  $\mathbf{w}(\omega)$  is gust downwash matrix, which is a function of frequency and the geometry of the aerodynamic model. And details of  $\bar{\mathbf{M}}$ ,  $\bar{\mathbf{D}}$ ,  $\bar{\mathbf{K}}$ ,  $\bar{\mathbf{Q}}_A$  and  $\bar{\mathbf{Q}}_g$  can be found in Appendix.

To obtain sufficient analysis accuracy when solving Eq.(4) in generalized coordinate system, only these modes that dominate the gust response and flutter characteristics are selected and included in the  $\boldsymbol{\phi}$ , which are normally a limited number of low order modes. As the result, the size of the Eq. (4) can be reduced significantly to gain computational efficiency.



In aircraft design, the gust velocity based on a discrete 1-cosine gust profile is expressed below.

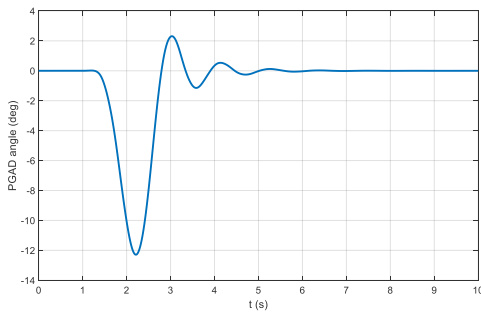
$$U = \begin{cases} \frac{U_{de}}{2} \left( 1 - \cos \frac{2\pi S}{2L_g} \right) & 0 \leq S \leq 2L_g \\ 0 & S > 2L_g \end{cases} \quad (6)$$

where  $U_{de}$  is the design gust velocity specified in airworthiness such as CS23 [27];  $L_g$  and  $S$  is the gust gradient (distance) and the distance of aircraft penetrating into the gust respectively. For example,  $S = V_c t$  at cruise speed  $V_c$ . Thus, the cosine term in Eq. (6) can also be expressed as  $\cos\left(\frac{2\pi V_c t}{2L_g}\right) = \cos(2\pi f_g t)$ , in which  $f_g = \frac{V_c}{2L_g}$  is an equivalent gust frequency (Hz).

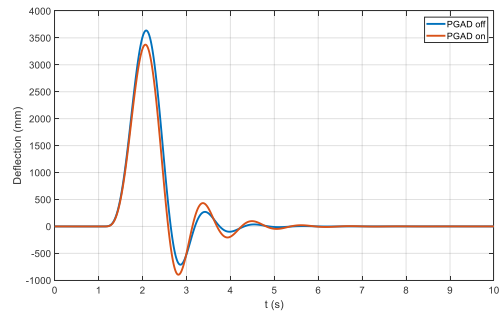
To keep in compliance with the CS-23 airworthiness [27], the most critical response case must be identified and evaluated in the range of gust gradient distances  $L_g = 9 \sim 107 \text{ m}$ , and a typical gust gradient is  $L_g = 12.5\bar{C}$ , where  $\bar{C}$  is the mean chord of the wing. In this case, the gust velocity can be calculated below.

$$U = \begin{cases} \frac{U_{de}}{2} \left( 1 - \cos \frac{2\pi S}{25\bar{C}} \right) & 0 \leq S \leq 25\bar{C} \\ 0 & S > 25\bar{C} \end{cases} \quad (7)$$

In the present study, two typical gust response cases are considered. In the first case A-1, the typical gust gradient for the aircraft is  $L_g = 12.5\bar{C} = 79.13 \text{ m}$ , and the equivalent gust frequency  $f_g = 0.65 \text{ Hz}$  according to the CS-23. For this critical case where the  $f_g$  is close to the first bending frequency  $0.70 \text{ Hz}$  of the wing, the gust response was calculated at flight speed Mach 0.3 with the maximum design gust velocity  $U_{de} = 17.07 \text{ m/s}$  at sea level. In response to the gust, the transverse deflection of the wing at span location  $Y=29.14 \text{ m}$  (interface with PGAD) are shown in Fig. 5. In response to the gust, the maximum rotation angle of the PGAD reached  $12.3^\circ$  as shown in Fig. 5 (a), and the wing deflection was reduced by 7.2% with the result as shown in Fig.5 (b). In the second case A-2, gust velocity  $U_{de} = 4.65 \text{ m/s}$  was set for the aircraft at flight speed Mach 0.31 and altitude  $4000 \text{ m}$ . The gust response results show the wing deflection reduced by 8.7% from  $813 \text{ mm}$  to  $742 \text{ mm}$  with maximum PGAD angle of  $3.1^\circ$  as presented in Fig. 5 (c) and (d).



(a)



(b)

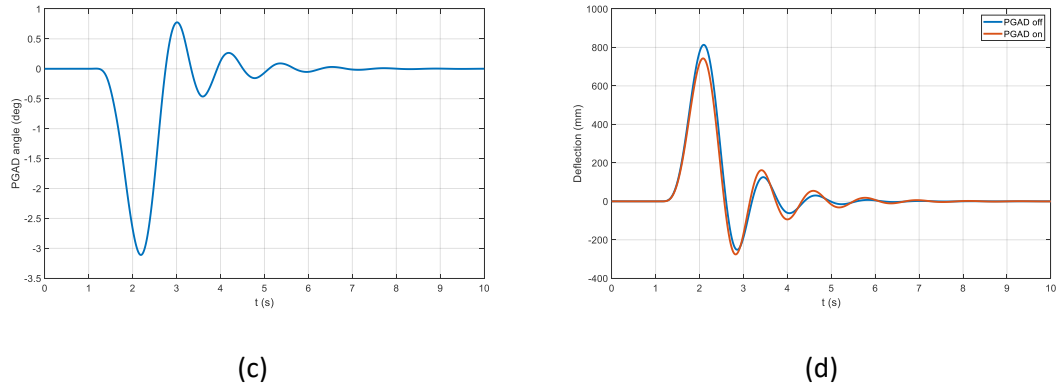


Figure 5. Gust response of the aircraft: (a) PGAD rotation angle and (b) wing deflection in case A-1, (c) PGAD rotation angle and (d) wing deflection at altitude of 4000m in case A-2.

### 3. The full-scale and reduced scale model of dynamical similarity

Aeroelastic scaling of a model needs to consider both aerodynamic and structural characteristics of the original model [21]. Aerodynamic scaling can be achieved by geometrically scaling the aerodynamic shape when Mach and Reynolds number is consistent. Structural similitude depends upon not only geometrically scaling the structural components but also material scaling requirement. In order to design a scaled wind tunnel test model that not only represents the aeroelastic behaviour of the full-scale model, but also can be realistically built, a beam-like model is usually adopted in practice instead of the original wing-box structure. This will not only simplify the scaling process, but also make the manufacture of the physical model feasible in practice. In the present investigation, a beam-like scaled model was selected. Therefore, the scaling process is divided into two steps, firstly the original FE model was simplified to a full-scale beam-like model that is of the same static and dynamic behaviour of the original one, namely Representative Beam Model (RBM); secondly a scaled RBM was designed according to the scaling factors. The details are presented in the following sections.

#### 3.1. A representative beam model and scaling results

To validate the gust alleviation analysis of the full-scale aircraft model, a scaled RBM was designed and manufactured for wind tunnel test. As described above, the design process of the scaled model is divided in two steps. In the first step, the original wing structure FE model was simplified to a full-scale Representative Beam Model (RBM). Based on the structural configuration of the aircraft as shown in Fig. 1, an FE model of the full-scale RBM was created as shown in Fig.6(a). The RBM takes twin-spar structural layout for inboard wing and a single spar layout for the outboard wing. The model keeps the same sectional bending and torsional rigidities as the original aircraft structure from root to tip along the span. The distributed mass in the FE model of the original aircraft structure was also simplified by reducing to limited number of lump mass in the RBM as shown in Fig.6(a). The concentrated mass of the pylon, engine, fuel and other systems were also included in the RBM according to their CG locations.

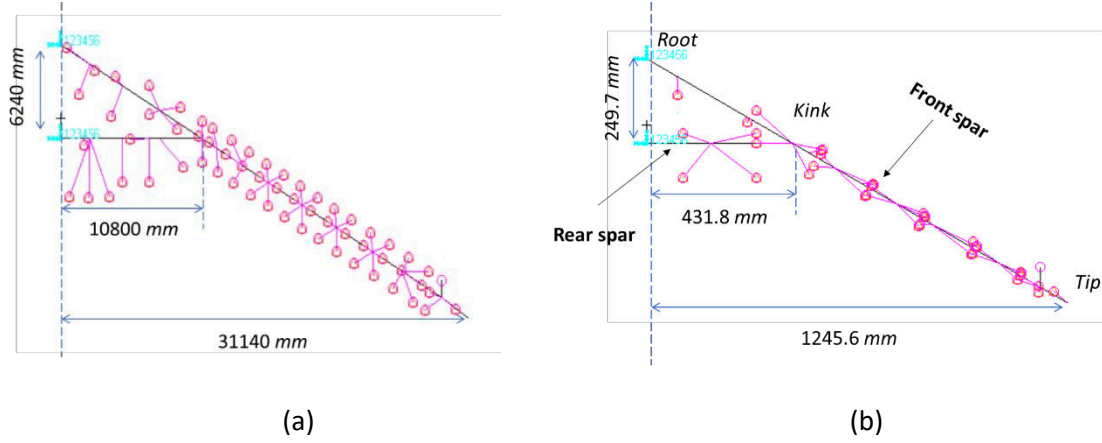


Figure 6. FE models of the (a) RBM and (b) scaled beam model

To ensure the original aircraft structure is best represented by the full-scale RBM, modal and flutter analysis of the RBM were performed and compared with the original aircraft structure model as shown in Table 6. The deviation of the first three modal frequencies of the full-scale RBM from the original aircraft model is less than 3%; the deviation of the higher order modes, the 3<sup>rd</sup> bending and 1<sup>st</sup> torsion frequency is 8.8% and 5.1% respectively. While the deviation of flutter speed and associated frequency ( $V_f = 262.7$  m/s and  $f_f = 3.04$  Hz) of the RBM is less than 6% from the results of the original aircraft model ( $V_f = 248.0$  m/s and  $f_f = 2.93$  Hz). The results indicate that the full-scale RBM provides a simplified and accurate alternative of the original aircraft model.

Table 6. Modal frequency and flutter speed of the original aircraft and the full-scale RBM

	Mode (Hz)					Flutter speed (m/s)
	1 <sup>st</sup> Bending	PGAD Rotation	2 <sup>nd</sup> Bending	3 <sup>rd</sup> Bending	1 <sup>st</sup> Torsion	
Original aircraft FE model	0.70	1.93	3.34	7.08	12.87	248.0
Full-scale RBM	0.68	1.95	3.36	7.70	12.21	262.7

In the second step of scaling process, a reduced scale model of the full-scale RBM can be created by applying the similitude theory as the basic scaling law. Dimensional analysis is a common methodology used to derive the similarity conditions and scale factors according to Coutinho et al [28]. In the analysis, the number of parameters is reduced by creating a set of dimensionless products, which are called  $\pi$ -terms in Buckingham  $Pi$  theorem. It states that a given relationship among  $n$  variables can be reduced to an equivalent relationship with a set of  $n-r$  dimensionless  $\pi$ -terms as expressed below, where  $r$  is the fundamental units included in the variables,

$$\Phi(\pi_1, \pi_2, \dots, \pi_{n-r}) = 0 \quad (8)$$

where  $\Phi$  is called functional relation, which is unnecessarily to be a known or explicit function of the system. If  $\pi_1$  involves the dependent variable for a system or specific phenomena, it can be rewritten as a function of the other independent  $\pi$ -terms,

$$\pi_1 = f(\pi_2, \dots, \pi_{n-r}) \quad (9)$$

Thus, a general expression for the reduced scale model, or called prototype, and the full-scale model can be written as

$$\pi_{1p} = f(\pi_{2p}, \dots, \pi_{(n-r)p}) \quad (10)$$

and

$$\pi_{1m} = f(\pi_{2m}, \dots, \pi_{(n-r)m}) \quad (11)$$

where the subscript  $p$  and  $m$  represents the prototype (reduced scale) model and full-scale model respectively.

If the following conditions are proved to be satisfied by analysis or test,

$$\begin{cases} \pi_{2p} = \pi_{2m} \\ \vdots \\ \pi_{(n-r)p} = \pi_{(n-r)m} \end{cases} \quad (12)$$

the reduced scale model is completely similar to the full-scale model, hence the following equations stand.

$$f(\pi_{2p}, \dots, \pi_{(n-r)p}) = f(\pi_{2m}, \dots, \pi_{(n-r)m}) \quad (13)$$

or  $\pi_{1p} = \pi_{1m}$

The equalities of  $\pi$ -terms in Eq. (12) guarantee the similarity of the pair of systems, hence are called similarity conditions or scaling laws.

For the flying-wing aircraft, the displacement ( $h$ ) depends on the length of wing ( $L$ ), density ( $\rho$ ), velocity ( $V$ ), mass ( $M$ ), mass moment of inertia ( $I_M$ ), spring rotational stiffness ( $K_\theta$ ), bending rigidity ( $EI$ ) or torsional rigidity ( $GJ$ ), and frequency  $\omega$  as expressed below.

$$h = f(L, \rho, V, M, I_M, K_\theta, EI, \omega) \quad (14)$$

When choosing the scale factors to build a physical model, the capability of the wind tunnel must be considered, such as the size, flow speed and air density. Hence, in the expression (14), the three repeating variables  $\rho$ ,  $L$  and  $V$  are selected as fundamental quantities; the unit of mass [ $M$ ], dimension [ $L$ ] and time [ $T$ ] taken as the basic unit. By applying Buckingham's theorem, Eq. (14) can be rewritten as

$$\frac{h}{L} = f\left(\frac{M}{\rho L^3}, \frac{I_M}{\rho L^5}, \frac{\omega L}{V}, \frac{EI}{\rho L^4 V^2}, \frac{K_\theta}{\rho L^3 V^2}\right) \quad (15)$$

so that the scaling laws for the aircraft are expressed as

$$\begin{cases} \left(\frac{M}{\rho L^3}\right)_p = \left(\frac{M}{\rho L^3}\right)_m \\ \left(\frac{I_M}{\rho L^5}\right)_p = \left(\frac{I_M}{\rho L^5}\right)_m \\ \left(\frac{\omega L}{V}\right)_p = \left(\frac{\omega L}{V}\right)_m \\ \left(\frac{EI}{\rho L^4 V^2}\right)_p = \left(\frac{EI}{\rho L^4 V^2}\right)_m \\ \left(\frac{K_\theta}{\rho L^3 V^2}\right)_p = \left(\frac{K_\theta}{\rho L^3 V^2}\right)_m \end{cases} \quad (16)$$

From the similarity condition  $\left(\frac{EI}{\rho L^4 V^2}\right)_p = \left(\frac{EI}{\rho L^4 V^2}\right)_m$  in Eq. (16), the relation of scale factors for bending rigidity  $\lambda_{EI} = (EI)_p/(EI)_m$  and the three repeating variables can be derived as follows,

$$\lambda_{EI} = \lambda_\rho \lambda_L^4 \lambda_V^2 \quad (17)$$

where  $\lambda_\rho = \rho_p/\rho_m$ ,  $\lambda_L = L_p/L_m$  and  $\lambda_V = V_p/V_m$ . Here we use  $\lambda_x$  denotes the scale factor of physical parameters  $x$ , which is a ratio of  $x$  between the prototype and the full-scale model.

Constrained by the size of the low-speed wind tunnel (5x4 ft), a 1:25 scale model was selected. As for the air density and velocity, the flight condition for the full-scale model at 4000m and Mach 0.3 was taken as the suitable reference. The air density is kept the same as that of the sea level, and the corresponding operating flow speed is around 20 m/s. The final result for density and velocity ratios adopted in the study are shown in Table 7. The similitude relations for other non-repeating variables can be also obtained in similar process with the results summarized in Table 7.

Table 7. Scale factors for a scaled representative beam model

	Scale factor	Symbol	Value
Repeating variables	Length ratio	$\lambda_L$	0.040
	Density ratio	$\lambda_\rho$	1.500
	Velocity ratio	$\lambda_V$	0.115
Non-repeating variable	Mass factor	$\lambda_M = \lambda_\rho \lambda_L^3$	9.600E-5
	Inertia factor	$\lambda_{I_M} = \lambda_\rho \lambda_L^5$	1.536E-7
	Rotation spring stiffness factor	$\lambda_{K_\theta} = \lambda_\rho \lambda_L^3 \lambda_V^2$	1.268E-6
	Section bending/torsion stiffness factor	$\lambda_{EI} = \lambda_\rho \lambda_L^4 \lambda_V^2$	5.073E-8
	Frequency factor	$\lambda_\omega = \lambda_V/\lambda_L$	2.874

According to the scale law, the ratio of length, density and velocity of the full-scale RBM to the scaled model were taken as the fundamental scale factors for the design of the scaled representative beam model (RBM), or scaled model in short. These factors and the theoretical solution of the scaled model were calculated as listed in Table 7.

Based on the scale factors listed in Table 7, an FE model of the 1:25 scaled beam-like model was created as shown in Fig.6 (b). The spar beam in rectangular cross-section was made of Aluminium alloy with Yong's modulus  $E = 72\text{GPa}$ , Poisson ratio  $\nu = 0.3$ , and density  $2700\text{ kg/m}^3$ . The dimensions of the beam with taped cross-section along the span were determined according to the required bending rigidity distribution set in the scaling law. The resulting geometric details are presented in Table 8.

Table 8. Dimensions of the spar cross sections of the scaled model

	Front spar			Rear spar	
	At root	At kink	At tip	At root	At kink
Width (mm)	62.3	15.0	5.6	54.8	15.0
Height (mm)	10.4	6.2	3.0	9.1	6.2

### 3.2. Reduced scale model manufacture and validation

According to the design details including the materials and dimensions, the 1:25 scaled model was manufactured. The spars as the primary structure of the model was first manufactured as shown in Fig. 7(a) based on the dimensions displayed in Table 8. The ribs and stringers, leading edge and trailing edge of the wing were also designed according to the scaling law to form a CAD model (half span) as shown in Fig. 7(b). The stringers were made of balsa wood, and the ribs were made of plywood board of thickness 1.5mm for light ribs and 3mm for heavy ribs based on the design. The leading and trailing edges were made of high-density foam to keep the aerofoil shape. These components were fabricated and assembled onto the spars to form the scaled physical model as shown in Fig. 7(c). Subsequently the model airframe was covered by the skin made of Ripmax Lightweight Covering Tissue. The PGAD included in the scaled model shown in Fig. 7(c) was also designed according to the scaling law and fabricated using the same foam as the leading edge. The PGAD shaft was located at 15% of the local chord measured from leading edge and mounted on the front spar through bearings and torsional spring at inboard extremity of the shaft. The PGAD can rotate depending upon the spring stiffness and external force within  $0\sim 20^\circ$  constraint.

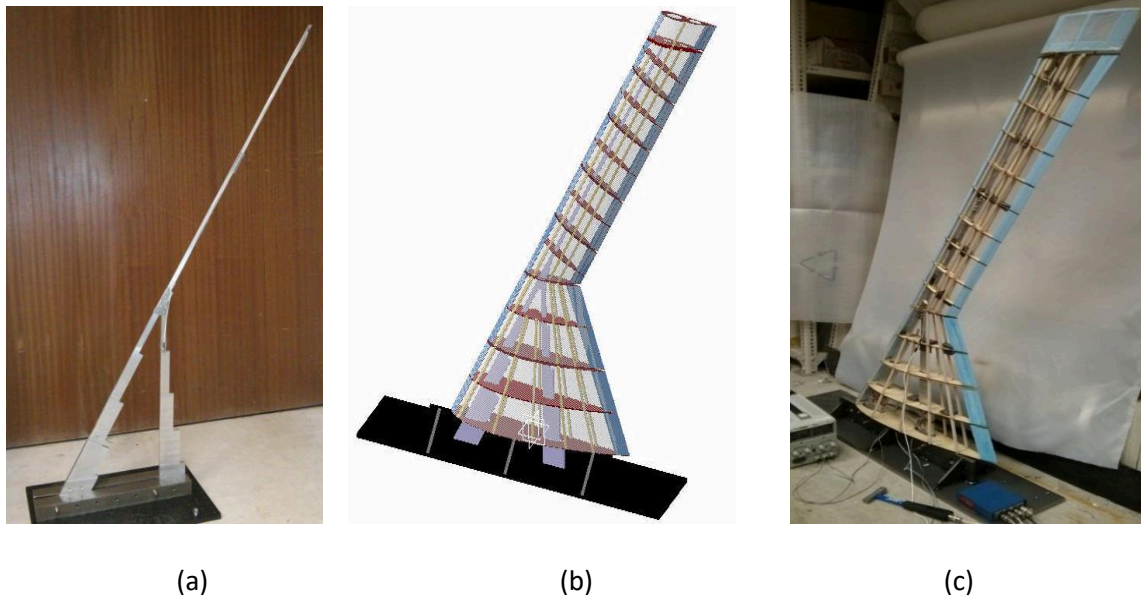


Figure 7. (a) manufactured spars (b) CAD model of the structure (c) assembled scaled model.

To verify the dynamic similarity of the scaled model as shown in Fig.6(b), the first three modes that dominant the gust response of the aircraft and flutter speed of the scaled RBM were compared with the theoretical solution obtained from the scaling law. As shown in Table 9, the maximum deviation of the first three modal frequencies between the scaled RBM and theoretical solution is less than 5.5%; the deviation of the 3<sup>rd</sup> bending and 1<sup>st</sup> torsion frequencies is 13.1% and 7.4% respectively. In addition,

the flutter speed  $V_f = 33.0$  m/s (flutter frequency  $f_f = 8.18$  Hz) of the scaled RBM is of 9% difference from the theoretical solution  $V_f = 30.2$  m/s ( $f_f = 8.85$  Hz) at sea level.

To verify the dynamic similarity of the scaled physical model as shown in Fig.7(c), vibration test was performed using an impact hammer modal testing kid with a commercial dynamic signal analyser. The averaging of multiple frequency response function (FRF) results were obtained using 10 impacts per measurement location. This resulted in a high quality of impacts during the measurement process. The force window was applied to the impact signal to reduce noise, and exponential window was used to filter the response signal. It was observed that the coherence overall was close to 1 across the relatively small and low frequency range from 0 to 60Hz. In the resulting FRF as shown in Fig. 8, the PGAD rotation mode was less clear than those modes of the wing model. This is probably due to the soft spring-shaft connection of the PGAD to model structure. The modal test results of the scaled RBM are displayed in Table 9.

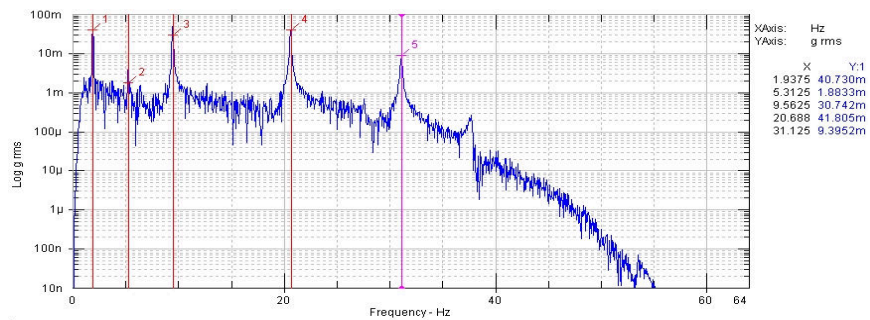


Figure 8. Frequency response function of the scaled test model

Table 9. Natural frequencies (Hz) of the reduced scale model

	Theoretical solution <sup>a</sup>	Scaled RBM (FE results)	Physical model (Test results)
1st Bending	1.96	1.94	1.94
PGAD Rotation	5.61	5.30	5.31
2nd Bending	9.66	9.43	9.56
3rd Bending	22.11	19.21	20.69
1st torsion	35.09	32.48	31.12

<sup>a</sup>. Theoretical solution of the scaled model is obtained from RBM according to the scaling law.

The deviation of the first three measured modal frequencies from the theoretical solution is less than 5.3%; while the deviation of the test data from the FE results of the scaled RBM is less than 1.4%; the deviation of the measured 3<sup>rd</sup> bending and 1<sup>st</sup> torsion mode from the theoretical solution is 7.7% and 4.2% respectively. Modal Assurance Criterion (MAC) was used to compare the mode shapes from theoretical solution and the scaled model to ensure the dynamic similarity. As shown in Fig.9, the MAC results of the first four modes is over 0.98; the MAC of the 1<sup>st</sup> torsion mode is 0.911. The results indicate that the scaled physical model is of high dynamic similarity and sufficient accuracy to represent the dynamic behaviour of the original full-scale aircraft model.



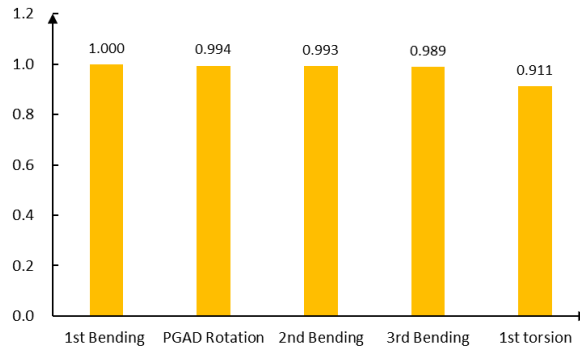
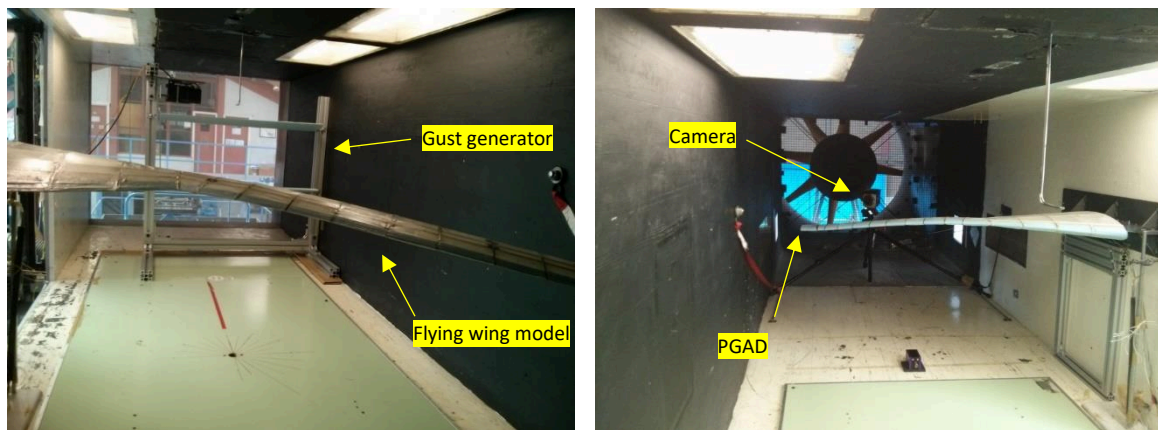


Figure 9. Modal Assurance Criterion between theoretical solution and scaled model

#### 4. Wind tunnel test of the scaled model

##### 4.1 Test setup and instrumentation

The experiment was conducted in a 5x4 ft open-circuit wind tunnel with maximum airflow speed 20m/s. The test model was set in horizontal position and mounted on the wall at the wing root as shown in Fig.10. A gust generator was mounted in the upstream of the wind tunnel to generate gust in sinusoidal profile as shown in Fig. 10(a). The gust generator was made of a couple of blades of NACA 0015 aerofoil with 0.2m chord and 1m span. The blades were driven by a brushless DC motor to rotate periodically in a range of angle amplitude  $\theta_b$  from  $0^\circ$  to  $\pm 20^\circ$ , and frequency  $f_b$  from 1Hz to 3Hz. An accelerometer was installed at the wingtip to record the acceleration in transverse direction. A high-speed camera was also located in the downstream as shown in Fig.10(b) to capture the dynamic deflection of the model in response to the gust during the wind tunnel test. The time history of the wing deflection and the PGAD rotation recorded by the high-speed camera were analysed by performing a digital post-process of the graphics.



(a)

(b)

Figure 10. Experimental setup in the wind-tunnel: (a) rear view, (b) front view.

##### 4.2. Wind tunnel test of the scaled physical model

In the first step of wind tunnel test, static wingtip deflection of -105mm due to the model gravity was measured at airflow velocity  $V=0$  that had less than 2% difference from -103mm wingtip deflection by FE analysis of the scaled physical model. In the second step, the model test was performed at different airflow velocity  $V=8, 10, 11.7m/s$  with the PGAD locked in neutral position. The measured



corresponding wingtip deflection was reduced from the original  $-105\text{mm}$  to  $-64.7\text{mm}$ ,  $-50.4\text{mm}$  and  $-36.7\text{mm}$  respectively. The resulting deflection difference was due to the applied aerodynamic force coupled with the elastic recovering force against the gravity of the model. In addition, a numerical model of the scaled physical model was created and validated by using the wind tunnel test data as shown in Fig. 11. The above test data and model was used as reference for gust response test in the next step.

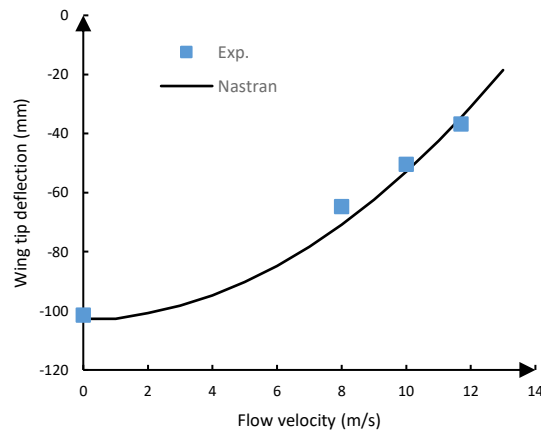


Figure 11. The wingtip deflections of the test model and FE analysis at different airflow velocity

In the third step of wind tunnel test, the PGAD effectiveness for gust alleviation at different airflow velocities in the range from  $V=8\text{m/s}$  to  $11.7\text{m/s}$  and gust velocity were evaluated. The gust generator was operated to produce gust of sinusoidal profile by rotating the blades at  $10^\circ \sim 15^\circ$  at a frequency from 1Hz to 3Hz to produce the required gust velocity.

In the first test case, the airflow velocity was set at  $8\text{m/s}$  and the blade rotating amplitude  $\theta_b = 10^\circ$  within the specified frequency range. The wingtip oscillating amplitude and acceleration were measured as shown in Fig. 12 (a) and (b). As shown in the results, the wingtip deflection peak value occurred at 2Hz, which was close to the 1st bending frequency (1.94 Hz) of the test model. By comparing the results with the PGAD on and off, it can be found that the wingtip deflection and acceleration at this critical frequency was reduced by 14.3% and 9.0% respectively when the PGAD was set in operation.

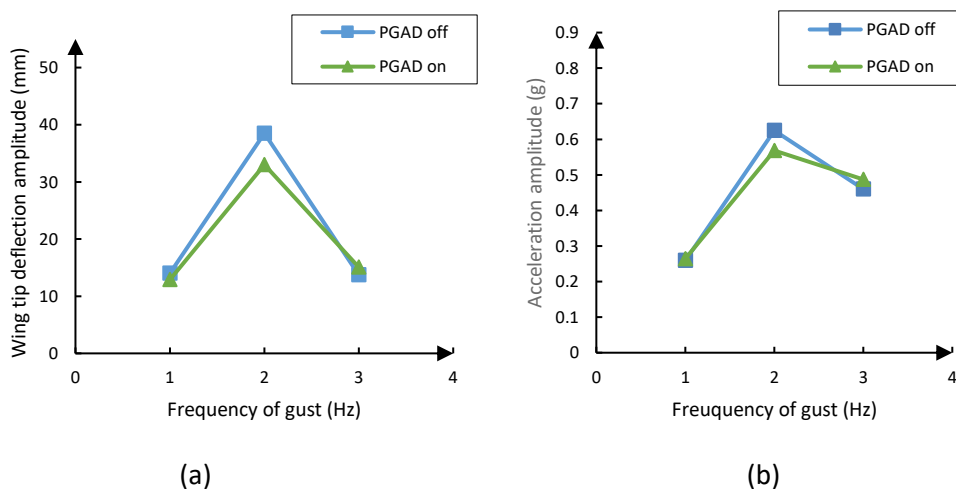


Figure 12. Gust response at airflow velocity  $8\text{ m/s}$  and blade rotating amplitude  $10^\circ$  at frequency 1Hz  $\sim$  3Hz: (a) wingtip deflection amplitude, (b) wingtip acceleration of the test model.

Further wind tunnel test was performed in the most critical case where the gust frequency is at 2Hz with different gust velocity  $U$  that depends upon the airflow velocity  $V$  and blade rotating amplitude  $\theta_b$ . The gust responses of the test model were measured at  $V=8m/s$ ,  $10m/s$  and  $11.7m/s$ , and the blade rotating amplitude  $\theta_b =10^\circ$  and  $15^\circ$  respectively. As shown in Fig. 13, the gust response in terms of wingtip deflection was reduced by 8.3%~14.3% with the PGAD rotating amplitude varying between  $4.0^\circ\sim 15.5^\circ$  under the  $20^\circ$  limit setting [14].

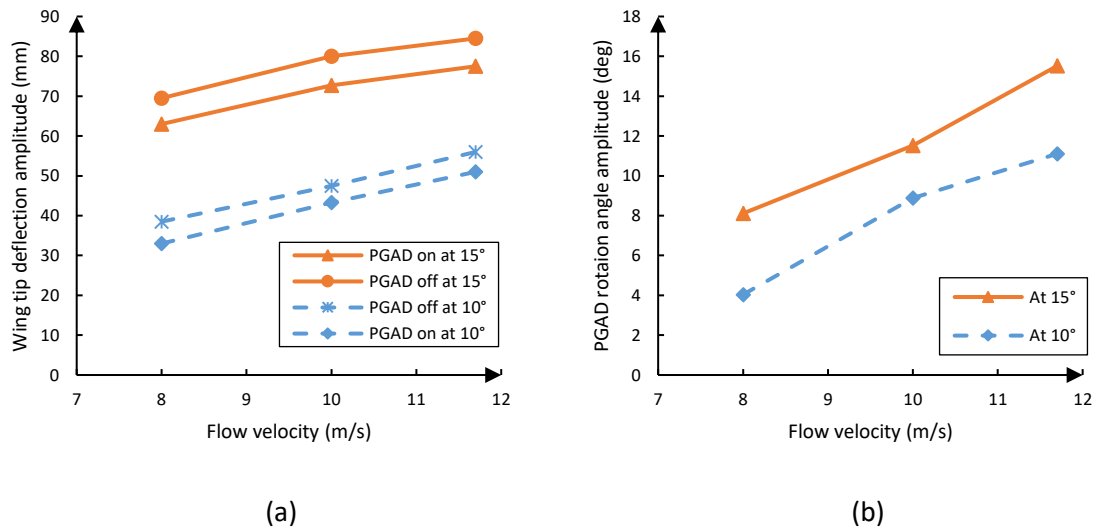


Figure 13. Wingtip deflection in response to gust generator blade rotating  $10^\circ$  and  $15^\circ$  at 2Hz: (a) with PGAD on and off, (b) corresponding PGAD rotating angle.

The test results show that the gust response varies with the airflow velocity  $V$  almost linearly for a constant blade rotation amplitude. This is because the gust load is proportional to  $V^2$  and the ratio of gust velocity to airflow velocity  $U/V$  [20]. The PGAD rotating amplitude increases with the  $V$  and  $U$ , which depends upon the blade rotating angle  $\theta_b$  of the gust generator. Consequently, the gust response and alleviation of the model with the PGAD in operation were also increased. However, the deflection reduction in percentage may not necessarily increase with the  $V$  and  $U$ . For example, the wingtip deflection was reduced by 5.5mm, 4.2mm and 5mm (14.3%, 8.8% and 8.9%) comparing with the PGAD off result in the case of  $\theta_b =10^\circ$  and  $V= 8m/s$ ,  $10m/s$  and  $11.7m/s$  respectively; when  $\theta_b$  was increased to  $15^\circ$ , the reduction value of the wingtip deflection was also increased by 6.5mm, 7.3mm and 7mm (9.3%, 9.1% and 8.3%). This behaviour is consistent with the effect of passive alleviation devices on manoeuvre performance [15] and handling quality [29].

The above wind tunnel test of the scaled model in the case of  $V= 11.7m/s$ ,  $U= 0.534m/s$  and  $\theta_b =15^\circ$  is corresponding to the case A-2 of the full-scale aircraft model according to the scaling law (see Fig.5(d)). In this particular case where the models have the best aeroelastic similarity, the gust response reduction by 8.3% measured in the wind tunnel test has very good agreement with the 8.7% gust response reduction of the full-scale model.

## 5. Conclusions

For the flying-wing aircraft with PGAD, numerical analysis shows that gust alleviation by 7~9% can be achieved in the range of gust velocity and frequency specified in CS-23. The PGAD effectiveness and validation of the analysis are demonstrated by wind tunnel test of a 1:25 scaled physical model. The scaled model can be designed according to the scaling law and manufactured as a representative of the original full-scale aircraft in dynamic similarity, which can be verified by experiment. In this case,

the maximum difference of the first three modes that dominant the gust response of the aircraft is less than 5.5% between the FE analysis, vibration test and the scaling law based theoretical solution of the physical model. The predicted flutter speed of the FE model is less than 9% difference from the theoretical solution. The verified scaled physical model of sufficient accuracy in dynamic similarity to the full-scale model can be used in a wind-tunnel test for gust response measurement.

In the wind tunnel test, a gust generator was manufactured and located in the upstream to produce gust velocity in sinusoidal profile in the range of frequency 1Hz ~ 3Hz. Similar to the full-scale aircraft, the most critical case appeared at gust frequency 2Hz that was close to the 1st bending mode of the scaled model (1.94Hz). The wind tunnel test shows that gust response was reduced by 8.3%~14.3% at gust frequency 2Hz and airflow velocity 8m/s ~ 11.7m/s with the PGAD oscillated at 4.0°~15.5°. The wind tunnel test conditions for the scaled model can be set to best represent a gust loading case of the full-scale aircraft according to the scaling law. For example, a wind tunnel test case for the scaled model was set according to the scaling law to represent the gust case A-2 for the full-scale aircraft. The difference of gust response and alleviation results of the two models in this case is less than 4.6%. The study presents an approach to design, build and validate a scaled model of dynamic similarity with the full-scale aircraft model to evaluate the PGAD effectiveness for gust alleviation by wind tunnel test.

## Appendix

The concrete form of the matrix in Section 2.3 is given as follows.

$$\bar{M} = \phi^T M \phi;$$

$$\bar{D} = \text{diag}\{\xi_1 \quad \dots \quad \xi_n\}, \text{ where } \xi \text{ is the modal damping coefficient};$$

$$\bar{K} = \phi^T K \phi;$$

$$\bar{Q}_A = \phi^T G^T S C_A^{-1} (D^1 + i k D^2) G \phi,$$

$$\bar{Q}_g = \phi^T G^T S C_A^{-1},$$

where  $G$  is the spline matrix to link the nodes of structural mesh and aerodynamic model,  $S$  and  $C_A$  represents the integration matrix and aerodynamic influence coefficient matrix respectively;  $D^1$  and  $D^2$  is real and imaginary parts of substantial differentiation matrix respectively;  $k = \omega b / V_\infty$  and  $b$  is the reduced frequency and reference semi-chord.

## Acknowledgements

The authors thank the USAF European Office of Aerospace Research and Development (EOARD) for financial support (grand award No. FA9550-14-0408), Prof. O.K. Sensburg at Cranfield University and Dr. Gregg Abate in EOARD and Dr. Raymond Kolony in USAF AFMC AFRL for their technical advice.

## References

- [1] E. Cestino, Design of solar high altitude long endurance aircraft for multi payload & operations, *Aerosp. Sci. Technol.* 10 (2006) 541–550. <https://doi.org/10.1016/j.ast.2006.06.001>.
- [2] C.L. Nickol, M.D. Guynn, L.L. Kohout, T.A. Ozoroski, High altitude long endurance air vehicle analysis of alternatives and technology requirements development, in: 45th AIAA Aerosp. Sci. Meet., 2007: pp. 12653–12669. <https://doi.org/10.2514/6.2007-1050>.

- [3] T.E. Noll, J.M. Brown, M.E. Perez-davis, S.D. Ishmael, G.C. Tiffany, M. Gaier, Investigation of the Helios Prototype Aircraft Mishap, Volume I: Mishap Report, in: NASA Tech. Reports, Langley Research Center, 2004.
- [4] G.J. Kennedy, J.R.R.A. Martinsy, A comparison of metallic and composite aircraft wings using aerostructural design optimization, in: 12th AIAA Aviat. Technol. Integr. Oper. Conf., 2012. <https://doi.org/10.2514/6.2012-5475>.
- [5] F. Abdelmoula, Design of an open-loop gust alleviation control system for airborne gravimetry, *Aerosp. Sci. Technol.* 3 (1999) 379–389. [https://doi.org/10.1016/S1270-9638\(00\)86428-7](https://doi.org/10.1016/S1270-9638(00)86428-7).
- [6] T.E. Disney, The C-5A active load alleviation system, in: *Aircr. Syst. Technol. Meet.*, AIAA, Los Angeles, California, USA, 1975. <https://doi.org/10.2514/6.1975-991>.
- [7] R.T. Britt, S.B. Jacobson, T.D. Arthurs, Aeroservoelastic analysis of the B-2 bomber, *J. Aircr.* 37 (2000) 745–752. <https://doi.org/10.2514/2.2674>.
- [8] T. de S.S. Versiani, F.J. Silvestre, A.B. Guimarães Neto, D.A. Rade, R.G. Annes da Silva, M. V. Donadon, R.M. Bertolin, G.C. Silva, Gust load alleviation in a flexible smart idealized wing, *Aerosp. Sci. Technol.* 86 (2019) 762–774. <https://doi.org/10.1016/j.ast.2019.01.058>.
- [9] M. Alam, M. Hromcik, T. Hanis, Active gust load alleviation system for flexible aircraft: Mixed feedforward/feedback approach, *Aerosp. Sci. Technol.* 41 (2015) 122–133. <https://doi.org/10.1016/j.ast.2014.12.020>.
- [10] Y. Li, N. Qin, Airfoil gust load alleviation by circulation control, *Aerosp. Sci. Technol.* 98 (2020) 105622. <https://doi.org/10.1016/j.ast.2019.105622>.
- [11] P. Roesch, R. Harlan, A passive gust alleviation system for light aircraft, in: *AIAA Mech. Control Flight Conf.*, AIAA, Anaheim, California, USA, 1974. <https://doi.org/10.2514/6.1974-773>.
- [12] S. Miller, G.A. Vio, J.E. Cooper, O. Sensburg, Optimisation of a scaled sensorcraft model with passive gust alleviation, 12th AIAA/ISSMO Multidiscip. Anal. Optim. Conf. MAO. (2008) 1–18. <https://doi.org/10.2514/6.2008-5875>.
- [13] S. Miller, G.A. Vio, J.E. Cooper, Development of an adaptive wing tip device, in: 50th AIAA/ASME/ASCE/AHS/ASC Struct. Struct. Dyn. Mater. Conf., AIAA, Palm Springs, California, USA, 2009: pp. 1–14. <https://doi.org/10.2514/6.2009-2121>.
- [14] S. Guo, Q. Fu, O.K. Sensburg, Optimal design of a passive gust alleviation device for a flying wing aircraft, in: 12th AIAA Aviat. Technol. Integr. Oper. Conf., AIAA, Indianapolis, Indiana, USA, 2012. <https://doi.org/10.2514/6.2012-5625>.
- [15] S. Guo, J.E. De Los Monteros, Y. Liu, Gust alleviation of a large aircraft with a passive twist wingtip, *Aerospace.* 2 (2015) 135–154. <https://doi.org/10.3390/aerospace2020135>.
- [16] A. Castrichini, V. Hodigere Siddaramaiah, D.E. Calderon, J.E. Cooper, T. Wilson, Y. Lemmens, Nonlinear folding wing tips for gust loads alleviation, *J. Aircr.* 53 (2016) 1391–1399. <https://doi.org/10.2514/1.C033474>.
- [17] A. Castrichini, J.E. Cooper, T. Wilson, A. Carrella, Y. Lemmens, Nonlinear negative stiffness wingtip spring device for gust loads alleviation, *J. Aircr.* 54 (2017) 627–641. <https://doi.org/10.2514/1.C033887>.

- [18] R.C.M. Cheung, D. Rezgui, J.E. Cooper, T. Wilson, Testing of a hinged wingtip device for gust loads alleviation, *J. Aircr.* 55 (2018) 2050–2067. <https://doi.org/10.2514/1.C034811>.
- [19] R.C.M. Cheung, D. Rezgui, J.E. Cooper, T. Wilson, Testing of folding wing-tip for gust load alleviation in high aspect ratio wing, *AIAA Scitech 2019 Forum*. (2019) 1–15. <https://doi.org/10.2514/6.2019-1863>.
- [20] S. Guo, Z.W. Jing, H. Li, W.T. Lei, Y.Y. He, Gust response and body freedom flutter of a flying-wing aircraft with a passive gust alleviation device, *Aerosp. Sci. Technol.* 70 (2017) 277–285. <https://doi.org/10.1016/j.ast.2017.08.008>.
- [21] R.L. Bisplinghoff, H. Ashley, R.L. Halfman, *Aeroelasticity*, Addison-Wesley Publishing Company, Cambridge, MA, 1955.
- [22] S. Yusuf, A. Pontillo, S. Weber, D. Hayes, M. Lone, Aeroelastic scaling for flexible high aspect ratio wings, in: *AIAA Scitech 2019 Forum*, 2019: pp. 1–15. <https://doi.org/10.2514/6.2019-1594>.
- [23] T.J. Allen, B.W. Sexton, M.J. Scott, SUGAR truss braced wing full scale aeroelastic analysis and dynamically scaled wind tunnel model development, in: *56th AIAA/ASCE/AHS/ASC Struct. Struct. Dyn. Mater. Conf.*, 2015: pp. 1–9. <https://doi.org/10.2514/6.2015-1171>.
- [24] M. French, F.E. Eastep, Aeroelastic model design using parameter identification, *J. Aircr.* 33 (1996) 198–202. <https://doi.org/10.2514/3.46922>.
- [25] A.P. Ricciardi, R.A. Canfield, M.J. Patil, N. Lindsley, Nonlinear aeroelastic scaled-model design, *J. Aircr.* 53 (2016) 20–32. <https://doi.org/10.2514/1.C033171>.
- [26] M. Cid Montoya, J.P.C. King, L. Kong, F. Nieto, S. Hernández, A method for improving the dynamic response of full bridge reduced-scale models in aeroelastic wind tunnel tests by using optimization algorithms, *J. Wind Eng. Ind. Aerodyn.* 167 (2017) 198–216. <https://doi.org/10.1016/j.jweia.2017.04.003>.
- [27] European Aviation Safety Agency, *Certification Specifications for Normal, Utility, Aerobatic, and Commuter Category Aeroplanes CS-23 Amendment 3*, 2012.
- [28] C.P. Coutinho, A.J. Baptista, J. Dias Rodrigues, Reduced scale models based on similitude theory: A review up to 2015, *Eng. Struct.* 119 (2016) 81–94. <https://doi.org/10.1016/j.engstruct.2016.04.016>.
- [29] A. Castrichini, T. Wilson, F. Saltari, F. Mastroddi, N. Viceconti, J.E. Cooper, Aeroelastics flight dynamics coupling effects of the semi-aeroelastic hinge device, *J. Aircr.* 57 (2020) 333. <https://doi.org/10.2514/1.C035602>.

# Passive gust alleviation of a flying-wing aircraft by analysis and wind-tunnel test of a scaled model in dynamic similarity

He, Shun

2021-03-29

Attribution-NonCommercial-NoDerivatives 4.0 International

---

He S, Guo S, Liu Y, Luo W. (2021) Passive gust alleviation of a flying-wing aircraft by analysis and wind-tunnel test of a scaled model in dynamic similarity. *Aerospace Science and Technology*, Volume 113, June 2021, Article number 106689

<https://doi.org/10.1016/j.ast.2021.106689>

*Downloaded from CERES Research Repository, Cranfield University*